

## Highlights

### **Differentiable Simulator for Electrically Reconfigurable Electromagnetic Structures**

Johannes Müller, Dennis Philipp, Matthias Günther

- Introducing the possibility of gpu-accelerated, parallel processing of resulting electromagnetic fields from any given scattering parameters ( $S_C$ ) and earlier preprocessing steps
- The precise control of the magnitude of the magnetic field normal to the center of each individual unit cell of three differently sized resonant structures is demonstrated using gradient-based optimization on a differentiable simulation

# Differentiable Simulator for Electrically Reconfigurable Electromagnetic Structures

Johannes Müller<sup>a,b</sup>, Dennis Philipp<sup>a,b</sup>, Matthias Günther<sup>a,b</sup>

*<sup>a</sup>Faculty of Physics, University of Bremen, Otto-Hahn-Allee  
1, Bremen, 28359, Bremen, Germany*

*<sup>b</sup>Fraunhofer MEVIS, Max-Von-Laue-Straße 2, Bremen, 28359, Bremen, Germany*

---

## Abstract

Electrically reconfigurable metasurfaces for MRI can exhibit many degrees-of-freedom. Each tunable parameter has an impact on the final response of the metasurface to an impinging magnetic field. Thus the configuration of the electric parameters have a significant impact on how metasurfaces shape the overall magnetic field distribution. Due to the high number of parameters and the mutual coupling, shaping the field in a desired way can be a non-trivial and time-consuming challenge.

This paper introduces a novel CUDA-enabled PyTorch-based framework designed for the gradient-based optimization of such reconfigurable electromagnetic structures with electrically tunable parameters. Traditional optimization techniques for these structures often rely on non-gradient-based methods, limiting efficiency and flexibility. Our framework leverages automatic differentiation, facilitating the application of gradient-based optimization methods. This approach is particularly advantageous for embedding within deep learning frameworks, enabling sophisticated optimization strategies.

We demonstrate the framework's effectiveness through comprehensive simulations involving resonant structures with tunable parameters. Key contributions include the efficient solution of the inverse problem. The framework's performance is validated using three different resonant structures: a single-loop copper wire (Unit-Cell) as well as an 8x1 and an 8x8 array of resonant unit cells with multiple inductively coupled unit cells (1d and 2d Metasurfaces). Results show precise control over the magnetic field's component normal to the surface of each resonant structure, achieving desired field strengths with minimal error. The proposed framework is compatible with existing simulation software.

This PyTorch-based framework sets the stage for advanced electromagnetic control strategies for resonant structures with application in e.g. MRI, providing a robust platform for further exploration and innovation in the design and optimization of resonant electromagnetic structures.

*Keywords:* , automatic differentiation, deep learning integration, differentiable simulation, electromagnetic structures, forward problem, gradient-based optimization, inverse problem, magnetic field control, MRI enhancement, PyTorch framework, reconfigurable metasurfaces, resonant structures, tunable parameters

---

## 1. Introduction

The application of properly configured resonant structures in MRI offers several advantages that significantly enhance imaging efficiency. Resonant electromagnetic structures, like e.g. metasurfaces (MTS) and metamaterials (MTMs), manipulate the magnetic field in a well-defined manner, leading to improved performance metrics such as enhanced signal-to-noise ratio (SNR), increased imaging resolution and reduced scanning time.

Resonant electromagnetic structures can be static, tunable, or reconfigurable. Static structures maintain constant properties over time. A significant enhancement in SNR [1], image resolution [1], and penetration depth [2, 3, 4] with preconfigured passive resonant structures are demonstrated. However, for specific use-cases, adjusting the behavior of these structures may be desirable to account for e.g. different loading conditions.

Electrically reconfigurable structures exhibit deliberately adjustable global behavior over time, allowing them to adapt to varying loading conditions [5] and to realize a spectral shift of the metasurface eigenmode [6]. They may also automatically detune in order to protect the patient against strong magnetic fields in transmit [7].

Reconfigurable resonant structures provide arbitrary spatio-temporal control over electromagnetic fields. Adjustment of the individual circuit parameters of these structures changes their behavior. Due to coupling, a local change in one cell can influence neighboring cells, making it challenging to accurately set proper parameters for a desired magnetic field distribution.

One of the first individually tunable resonant unit cells is presented in Ref. [8] highlighting the importance over finely-grained reconfigurability. Various tuning strategies, including electrical, optical, thermal, and mechanical

adjustments, have been implemented for different applications [9, 10]. The potential of reconfigurable metasurfaces in MRI is demonstrated firstly by Wang [11], where the SNR in a 3T MRI is selectively boosted by up to 28 times. A prototype with 14 degrees-of-freedom is proposed [12, 13, 14].

The capacitances  $C$  of reconfigurable electromagnetic structures and the resulting total magnetic field  $B$  are related such that the mapping  $C \rightarrow B$  can be considered a forward problem. This relationship can be observed analytically, numerically, and experimentally. The circuit model combined with the Biot-Savart law, can be used if the structure is small compared to the wavelength. Analytical modeling is possible but not agnostic to the resonant structure’s geometry. One model therefore does not fit all resonant structures and possibly cannot be reused for different structures.

The inversion of Biot-Savart in itself is in many cases challenging and can be inaccurate [15]. In some cases it is posed as an optimization problem [16]. To the best of the authors knowledge there is no analytical solution to the inverse of the Biot-Savart law for more complicated structures.

The objective of this study is to find a method that leverages the capability of reconfigurable resonant structures and allows the extraction of parameters that realize a desired electromagnetic field component, e.g.,  $|B_z|$  at a given point in space.

### 1.1. Context

Resonant structures as e.g. reconfigurable metasurfaces, exhibit many degrees-of-freedom that allow the targeted modification of a resulting magnetic field in e.g. MRI and therefore the adaption to a specific imaging goal and different loading conditions.

Simulations play a critical role in the analysis of interactions between electromagnetic fields, objects, resonant structures, and associated circuitry. Circuitry can significantly alter the resonant behavior of electromagnetic structures, thereby affecting the resulting electromagnetic fields. This interaction requires detailed analysis, which is why commercial software solutions such as Dassault Systèmes CST Microwave Studio (CST MWS) include comprehensive simulation capabilities.

While simulators embedded in commercial software offer robust tools for analysis, they often lack cost-efficient, standalone optimization of electrically tunable parameters. This limitation has led to the development and adoption of open-source solutions, particularly in Matlab and Python environments. These solutions enable cost-effective, standalone calculations of

electromagnetic fields concerning circuit parameters, providing a more flexible and accessible approach for researchers and engineers.

There exists a Matlab-based solution [17] which can be used with non-gradient-based optimization techniques, such as the Self-Organizing Migrating Algorithm (SOMA) or the `fminsearch` function.

Similarly, an extensive Python-based circuit-cosimulation framework is introduced [18]. This framework supports both 1-port and 2-port networks and leverages `numpy`. However, a key limitation is the inability to perform gradient-based optimization due to the lack of automatic differentiation support in these packages.

Other optimization techniques for resonant structures have been explored, as in Ref. [19]. While this algorithm offers an efficient way for the control of the current phases in the structure, it is not applicable to certain structures. It also does not explicitly focus on optimization of the magnetic or electric field.

## *1.2. Novelty*

We propose a PyTorch-based framework that leverages automatic differentiation to facilitate the use of gradient-based optimization methods for tuning circuit parameters within electromagnetic simulations. This approach is particularly compelling due to its potential for embedding within deep-learning frameworks, enabling sophisticated optimization strategies.

The power of neural networks lies in their ability to learn from data in the process of backpropagation, in which gradients of the loss function are propagated backwards through the network to update the weights. By employing a framework that inherently supports automatic differentiation, we can extend this powerful learning mechanism to the realm of electromagnetic simulation, thus opening up new avenues for research and application in the optimization of circuit parameters.

### *1.2.1. Advantages and Limitations*

The proposed framework enables efficient calculation of steady-state electric and magnetic fields in all three cartesian field components, enabling potential direct control over chosen fields respecting physics laws. The computational effort required is linearly dependent on the number of datapoints and ports, which enhances scalability and performance [20]. Furthermore, the framework is agnostic to both, simulation software and geometry, eliminating the need for analytical modeling. Integration with PyTorch allows for the

usage of PyTorch workflows and the incorporation of standard MLOps packages (e.g. mlflow), thereby facilitating streamlined and robust optimization processes.

## 2. Methods

A Full-wave electromagnetic (EM) multiport simulation accurately models the behaviour of complex electromagnetic systems. The simulation process involves the individual excitation of the system through multiple ports, each treated as an impedance element — a current source with an inner impedance capable of both exciting and absorbing power [21]. During simulation, the current source becomes active, stimulating each port individually. S-Matrix and EM fields of the systems response are exported, providing insight into the interaction of individual inputs with respect to the outputs of the system.

The resulting data encompasses the multi-port S-Parameter matrix and 3D electromagnetic fields, representing the system’s behaviour. The S-Parameters and EM fields can then be used for subsequent analysis leveraging the capabilities of tools like CoSimPy [18] or the framework presented in this paper. The calculations in this framework are based on the method proposed in [18] and therefore also follows the similar definitions if suitable. In the following, the S-Matrix extracted from the simulation software that contains the scattering parameters of the unconnected resonant structure shall be named  $\mathbf{S}_0$  the exported fields can be either  $B$  or  $H$  and  $D$  or  $E$ .

The circuitry needs to be modelled too. In this paper, RC circuits will be used. They can be modelled by

$$\mathbf{z}_C = \mathbf{R} - j \frac{1}{\omega \mathbf{C}}, \quad (1)$$

which relates to the S-parameters  $\mathbf{S}$  using

$$\mathbf{s} = \frac{\mathbf{z}_C - \mathbf{z}_0}{\mathbf{z}_C + \mathbf{z}_0}, \quad (2)$$

with  $\mathbf{s}, \mathbf{z}_C, \mathbf{C} \in \mathbb{C}^{n_{batch} \times n_f \times n_0}$ .

$\mathbf{z}_0$  is the characteristic impedance of the individual ports. For sake of simplicity one can assume  $n_f = n_{batch} \stackrel{!}{=} 1$  and omit these dimensions in the following.

The circuitry needs to be connected to the modelled resonant structure. Therefore a new tensor  $\mathbf{S}_C \in \mathbb{C}^{n_0+n_1 \times n_0+n_1}$  is build that can be separated into four parts [18]. See Fig. 1.

- $\mathbf{S}_{C_{11}} \in \mathbb{C}^{n_0 \times n_0}$  represents the reflection from the output perspective of the networks that connect to the resonant structure.
- $\mathbf{S}_{C_{22}} \in \mathbb{C}^{n_1 \times n_1}$  represents the reflection from the input perspective of the networks that connect to the resonant structure.
- $\mathbf{S}_{C_{12}} \in \mathbb{C}^{n_0 \times n_1}$ ,  $\mathbf{S}_{C_{21}} \in \mathbb{C}^{n_1 \times n_0}$  represent the transmission from input to output and vice-versa.

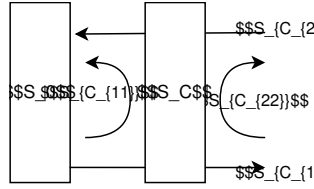


Figure 1: Visualization of the connection of the networks contained in  $\mathbf{S}_C$  to the resonant structure  $\mathbf{S}_0$ .

$n_0$  is being assigned to the number of ports of the resonant structure ( $\mathbf{S}_0$ ) and  $n_1$  being assigned to the number of external ports ( $\mathbf{S}_C$ ).

As a simplified example: For 1-port networks only values on the diagonal of  $\mathbf{S}_{C_{11}}$  are assigned as we connect the output-side to the resonant structure. These can only reflect power to a certain degree on this one port and do not transmit energy to the input ports of  $\mathbf{S}_C$ .

For the calculation of the resulting fields it is critical to consider the incident power on each individual port. As already described in [18], the complex incident voltage wave on each port can be given as

$$\mathbf{V}_{i,j} = \frac{\mathbf{V}_{i_{excitation}}}{-\mathbf{V}_{r_{system\_reflection}}} = \frac{\mathbf{S}_{C_{12}} \sqrt{Z'_{0,j} P}}{(\mathbf{I} - \mathbf{S}_{C_{11}} \mathbf{S}_0)} \quad (3)$$

$P$  is often assumed to be 1W. This assumption will also be made for the results generated in the following.  $I$  is the identity matrix.  $Z'_{0,j}$  is the characteristic impedance at the excitation. The index  $i$  stands for incident,  $r$  for reflected wave and  $j$  for number of excitation port. In this case  $j = 1$ .

We therefore get the net voltage-wave at each port of the resonant structure after interaction with the supporting circuitry and the resonant structure itself.

The power at each port can then be derived from the net voltage wave as follows [18]:

$$\mathbf{P}_{\text{inc}} = \frac{|\mathbf{V}_{\text{inc}}|^2}{\mathbf{Z}_0} \quad (4)$$

$\mathbf{P}_{\text{inc}}$  can then be used to linearly superimpose the individual electric or magnetic fields w.r.t. their amplitude and phase to one common electric or magnetic field [20]. For e.g. the B-field it can be described as follows:

$$\mathbf{B}_{\text{combined}} = \mathbf{B} \sqrt{|\mathbf{P}_{\text{inc}}|} e^{j\angle \mathbf{P}_{\text{inc}}} \quad (5)$$

With  $\mathbf{P}_{\text{inc}}$  being a  $(n_0, n_1)$  matrix and the Field e.g.  $\mathbf{B}_{\text{combined}}$  being a  $(n_1, 3, n_{\text{points}})$  tensor.

### 2.1. Optimization Pipeline

The variable  $\mathbf{S}_{\mathbf{C}}$  represents an intermediate multiport network (comparable to [18]) that manages the connection from the resonant structure ( $\mathbf{S}_0$ ) with its  $n_0$  ports to the output ports of the structure connected to circuitry ( $n_1$ ). The scattering tensor  $\mathbf{S}_{\mathbf{C}}$  therefore links the resonant structure to the networks.

The optimization pipeline allows for the optimization of any arbitrary S-parameter within the  $\mathbf{S}_{\mathbf{C}}$  tensor. The pipeline is therefore designed to offer maximum flexibility in defining custom preprocessing steps:

1. **User-Defined Preprocessing:** User-defined preprocessing of data that results in S-parameters. The user can build any desired preprocessing step that relates to the individual elements of  $\mathbf{S}_{C_{\text{var}}}$ . The custom preprocessing step must output a three-dimensional tensor  $(n_{\text{batch}}, n_f, n_{s\text{-params}})$ . The user defines the *indices* that map each element of this output tensor to corresponding positions in the  $\mathbf{S}_{C_{\text{var}}}$  tensor. *indices* contains two tensors with indices for  $x$  and  $y$  position assignment in  $\mathbf{S}_{C_{\text{var}}}$ . The first tensor contains the indices for rows ( $x$ ), and the second contains the indices for columns ( $y$ ). This ensures that the zero-valued  $\mathbf{S}_{C_{\text{var}}}$  tensor is populated with the relevant values, as determined by the user-defined indices.
2. **Constant S-parameter Definition:** Users also define an  $\mathbf{S}_{C_{\text{const}}}$  tensor containing constant S-parameters that remain unchanged during optimization. This allows for portions of the multiport network to stay fixed, while other parts (defined by  $\mathbf{S}_{C_{\text{var}}}$ ) are optimized.



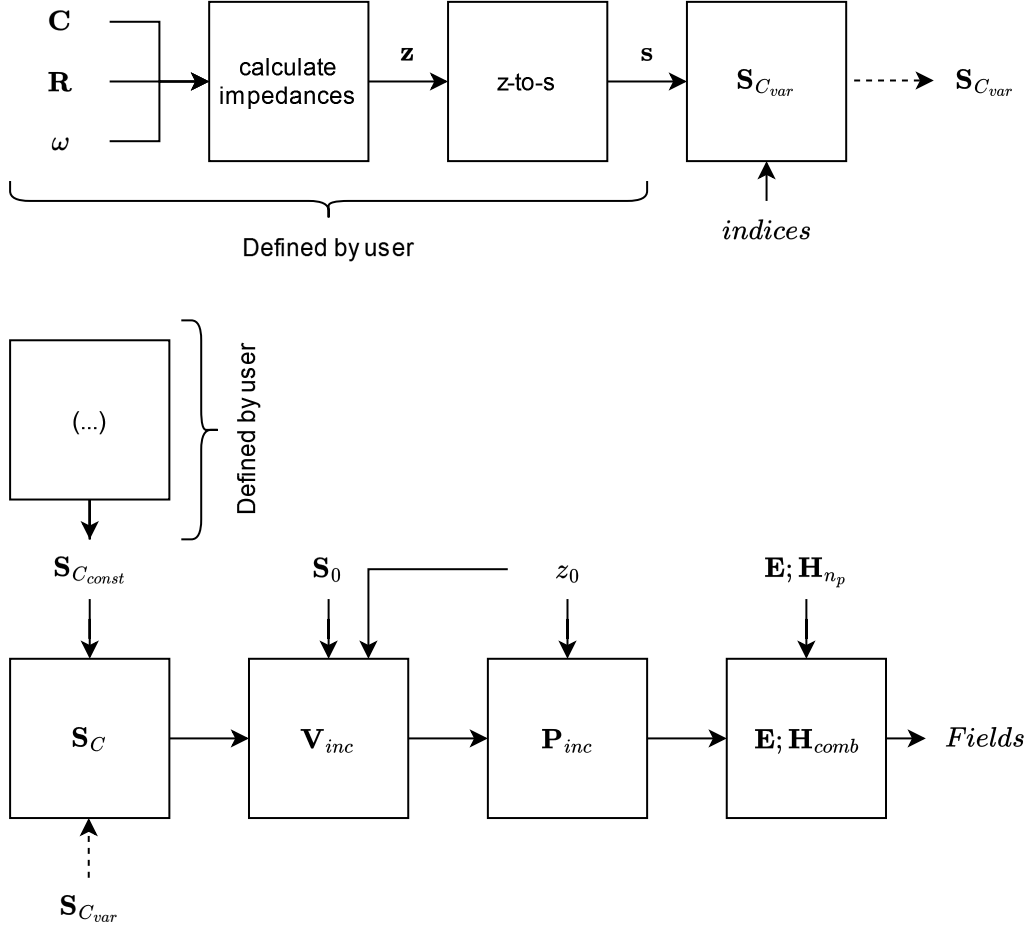


Figure 2: The fundamental pipeline calculates fields from given variables  $\mathbf{S}_C$  and  $\mathbf{S}_0$  as well as the fields that shall be combined  $\mathbf{E}_{n_p}, \mathbf{H}_{n_p}$ . The user can freely choose how to pass the individual elements of  $\mathbf{S}_C$  to the fundamental pipeline. In this case it might be useful to map specific circuit parameters to individual elements of  $\mathbf{S}_C$ . Therefore a preprocessing procedure is written and used in combination with the fundamental calculation pipeline.

- 3. Combination of  $\mathbf{S}_{Cvar}$  and  $\mathbf{S}_{Cconst}$ :** The framework then adds the  $\mathbf{S}_{Cvar}$  and  $\mathbf{S}_{Cconst}$  tensors. This creates the complete  $\mathbf{S}_C$  tensor that defines the behavior of the multiport network in the simulation.
- 4. Field Combination and Simulation:** After constructing the  $\mathbf{S}_C$  tensor, the pipeline proceeds with the field calculations, ultimately combining the electromagnetic fields as part of the final simulation

output.

## 2.2. Numerical Setup

The structure can be modelled using a full-wave electromagnetic solver toolkit such as Sim4Life [22] or CST MWS.

In the following example, three different resonant structures are constructed and simulated in a multiport simulation utilizing the Frequency Domain solver in CST MWS 2024. All structures are based on coupled split-ring geometries with different unit-cell sizes or a different number of cells. In order to demonstrate the versatility of the framework, they will be excited in two different ways: An untuned 1-port excitation coil and a tuned 2-port birdcage coil. The chosen simulation frequency is the Larmor frequency of proton MRI at 2.9 Tesla, which corresponds to approximately 123.5 MHz. All the cells have a wire width of 1 mm on FR-4 substrate. They rest on a phantom ( $\varepsilon = 70$ ;  $\sigma = 0.7S/m$ ) that introduces loading. The magnetic field component extracted is always the component normal to the surface of the resonant structure.

The first resonant structure consists of a single loop copper wire with an inner radius of 30 mm that is split by one port. A second port is connected to a PEC loop coil with an outer radius of 45 mm and a wire diameter of 1 mm that shall drive the resonant structure during cosimulation with 1W. The first port will be connected to a tunable RC-series network. The setup is shown in Fig. 3.

The second resonant structure contains a 1x8 line of coupled unit-cells with an outer-diameter of 28 mm and a centre-to-centre distance of 30mm. It will be exposed to a circularly polarized magnetic field generated by a tuned 2-port Birdcagecoil connected to two discrete ports. The two discrete ports are powered with 1W and a phaseshift of  $90^\circ$  to one another. The setup is shown in Fig. 4.

For the third structure the 1d-line is extended to 8x8 allowing more degrees of freedom in shaping the field in space. While the second structure is excited by a tuned birdcage coil, the 8x8 structure will be excited by an excitation coil with a diameter of 300 mm which is located at a distance of 150 mm above the substrate. The complete setup can be seen in Fig. 5.

## 2.3. Optimization configuration

For the first resonant structure, the magnetic field is measured at a distance of  $z = -30mm$ . For the other resonant structures the points of interest are

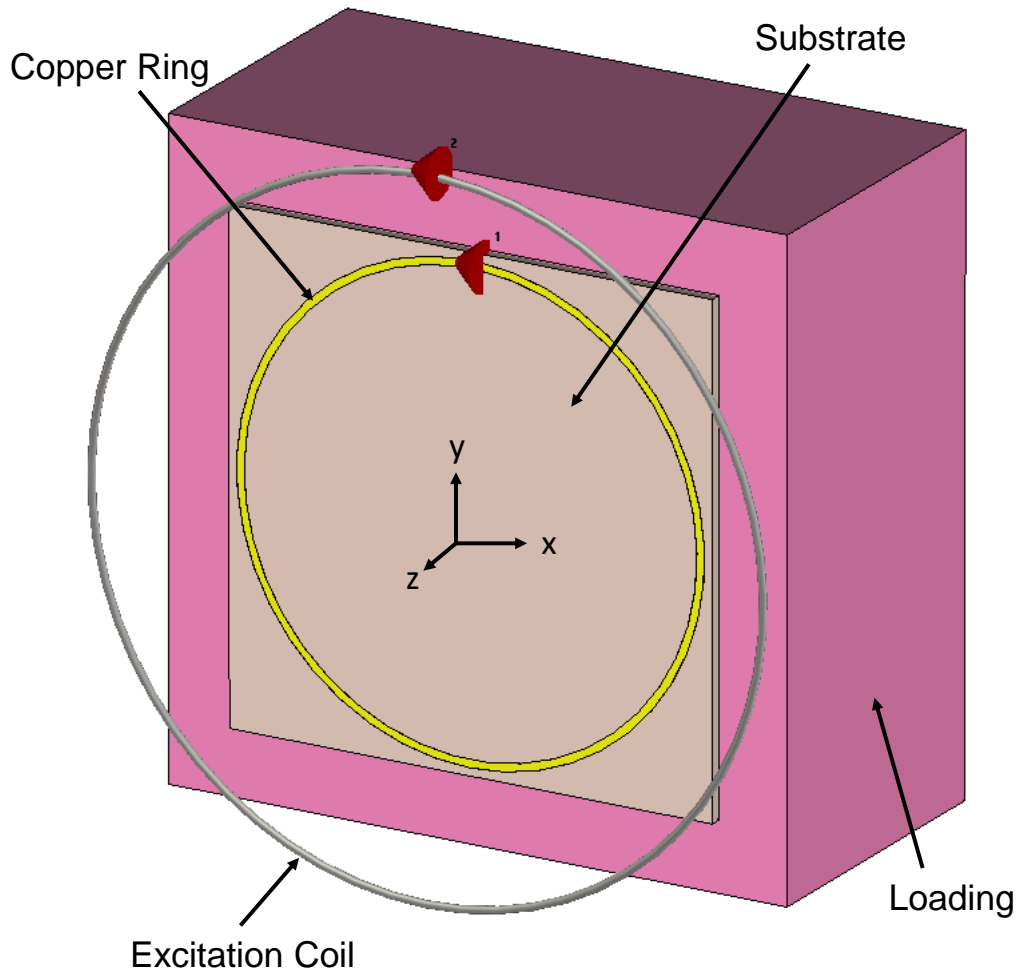


Figure 3: 0D single-cell resonant structure with one tuning network. The structure rests on a phantom. Port 1 will be connected to a tunable RC-network. The PEC excitation loop coil is driven by port 2. The coil excites the resonant structure during cosimulation.

located precisely at the center of each unit cell, offset by 0.8 times the cell diameter within the phantom. For a configuration with 8 unit cells, this yields 8 distinct points of interest. Similarly, for a system consisting of 64 unit cells, 64 distinct points of interest are obtained, each uniquely positioned within its respective cell. The points of interest will also be called collocation points when discussing the optimization problem.

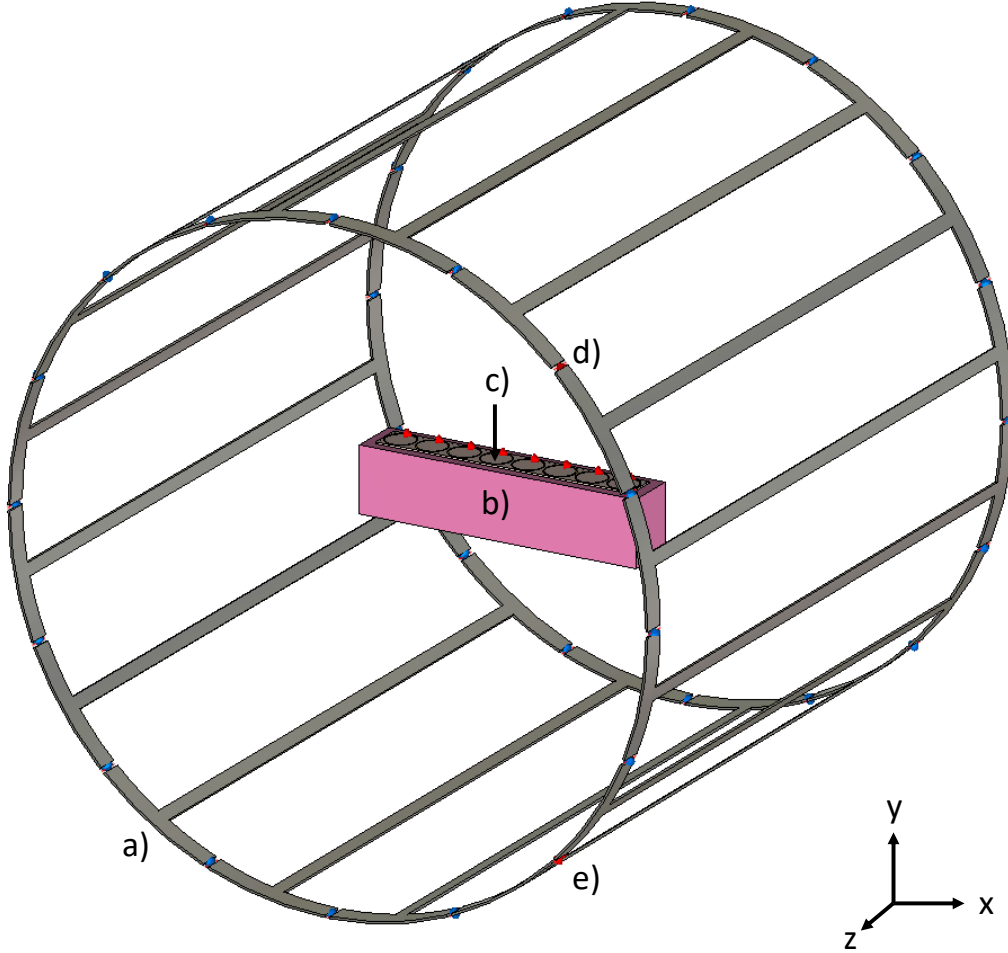


Figure 4: 1D resonant structure exposed to a circularly polarized magnetic field of a birdcage coil a). Ports 1-2 (d)-e)) are connected to the birdcage coil and driven with a  $90^\circ$  phase shift to one another. The remaining 8 ports of the resonant structure c) are connected to 1-port RC-Networks. The resonant structure is loaded b). The RF-shielding is hidden in order to allow the reader a complete view on the setup.

During the gradient-descent-based optimization, the Adam optimizer is utilized with a maximum of 2000 epochs and a learning rate of  $1 \times 10^{-13}$ . The Adam optimizer, a standard method commonly used in deep learning, offers features such as an adaptive learning rate and momentum [23]. The

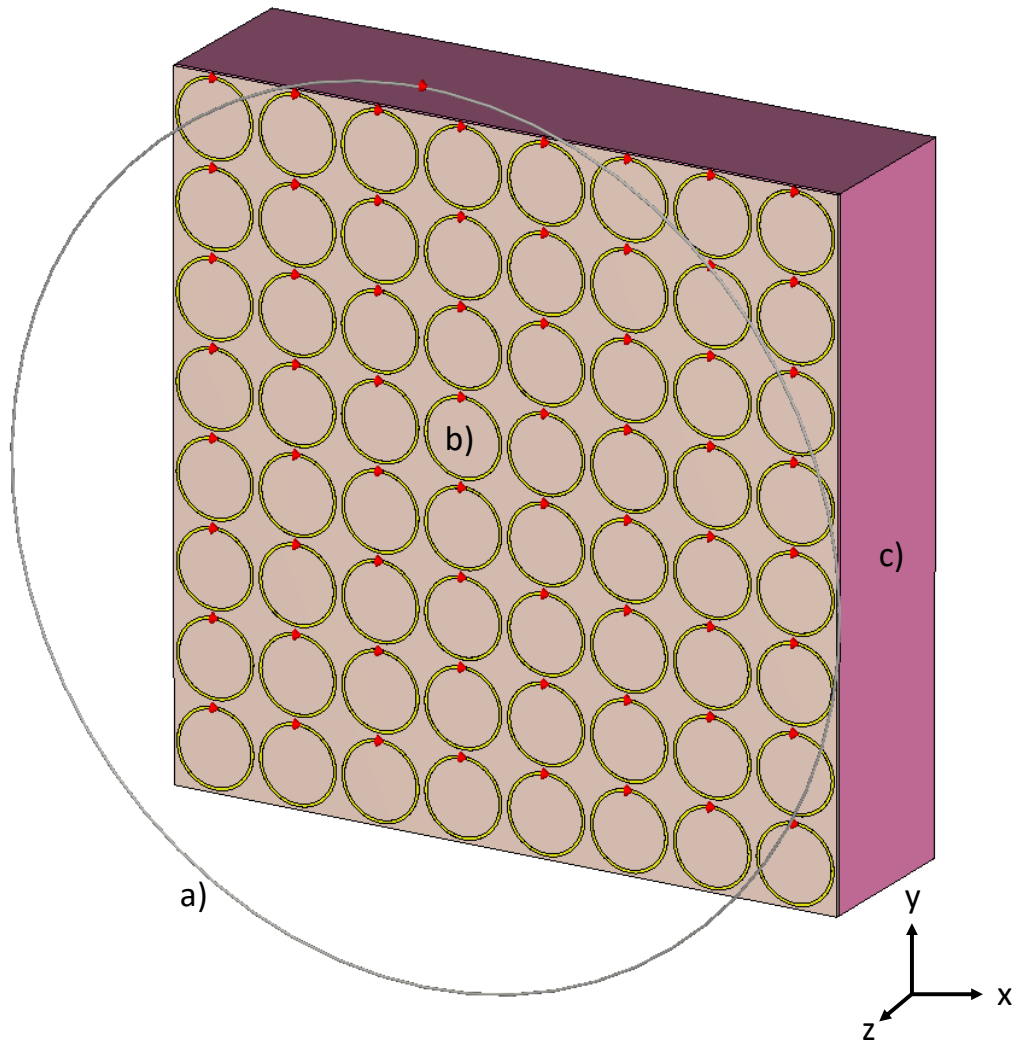


Figure 5: 2D resonant structure b) exposed to the magnetic field of an excitation coil a). Port 1 is connected to the excitation coil. The resonant structure is loaded c). The remaining 64 ports are connected to 1-port RC-Networks.

performance is evaluated using the Mean-squared-error (MSE). The optimization is conducted using CPU-only to ensure exact reproducibility. The used CPU for the Optimization is an Intel Core i7 13700KF together with 64 GB Ram. GPU-based acceleration can be used as well. In order to ensure exact reproducibility, no GPU is used at this time.

### 3. Problem Statement

The proposed framework allows to efficiently solve the forward problem  $C \mapsto B$ . As the equation  $B = \mu H$  holds and a phantom of permeability  $\mu_r = 1$  is used, the following results will relate to the  $H$ -field. By using gradient-descent based optimization, it offers the possibility to efficiently tackle the inverse problem  $H \mapsto C$ .

The central research question that shall be tackled using the presented framework can be formulated as follows: **Is it possible to infer the circuit parameters  $C$  of a 0D, 1D and 2D-resonant structure that together cause a desired magnetic field distribution.** The desired magnetic field strength in each point of space is called  $|H|$  while the realized magnetic field strength is  $|\hat{H}|$ .

The problem under investigation is an inverse problem. Inverse problems can be well or ill-posed. Hadamard defined a well-posed problem as a problem that has to fulfill the following widely known criteria:

1. existing solution
2. unique solution
3. continuous dependence on input data

A problem is ill-posed if one or more of the criterias are infringed.

### 4. Results

#### 4.1. Reconfigurable 0D Unit-Cell Optimization

The goal is to find a  $C$  that realizes a desired magnetic field strength  $|H_z|$  at  $z = -30$  mm. For the structure with only one tunable parameter this is a simple one dimensional map  $C \mapsto |H_z|$  of the form  $f : \mathbb{R} \mapsto \mathbb{R}$ . . Because of the simplicity of the problem it can be solved analytically.

The system model of a simple capacitively loaded Ring (CLR) without excitation can be described as follows:

$$Z = R + j\omega L - j\frac{1}{\omega C} \quad (6)$$

In resonance,  $Im\{Z\} = 0$  holds. The inductance  $L$  can be extracted from simulation. Therefore, one can solve for  $C_r$  as follows:

$$C_r = \frac{1}{\omega^2 L} = 8.39 \text{ pF}. \quad (7)$$

In order to use plausible values for  $|H_z|$ , arbitrarily chosen extreme capacitances 0.1 pF and 30 pF are extracted as well. For the lower boundary the minimum case of the two is chosen which results in a magnetic field strength of around 0.2 A/m. Then, 100 equidistantly distributed desired field strengths within 0.2 to 2.3 A/m are optimized for.  $|H_z| = 2.3$  A/m is being chosen for the upper bound as this is the magnetic field strength at resonance.

Using  $C_r$  as initial parameter, an overall MSE of  $1.09 \times 10^{-6}$  at epoch = 2000 is achieved. The error can be further reduced to  $8.03 \times 10^{-18}$  for the epoch with the lowest overall error (epoch=931). In tendency a longer optimization time results into a better convergence. Due to the nature of the adam optimizer the end result is still subject to fluctuation.

#### 4.2. Reconfigurable 1D MTS Optimization

In the following,  $|H_y|_{MTS}$  (simulation with resonant structure) is optimized relative to  $|H_y|_{ref}$  (simulation without resonant structure). Therefore, the optimization is conducted directly on the magnetic field enhancement factor in order to show a broader applicability of the algorithm on different scales. The enhancement factor shall be defined as:

$$\beta = \frac{|H_y|_{MTS}}{|H_y|_{ref}} \quad (8)$$

In practical cases, areas with stronger and weaker field strengths shall be realized locally. Therefore, the individual parameters of a resonant structure with eight inductively coupled unit cells are tuned so that the resulting  $\beta$  is optimized.  $\beta$  shall be modified so that following five cases can be demonstrated:

1. Peak
2. Trough
3. Hadamard Pattern
4. Homogenization
5. Arbitrary Field Shaping

1000 exemplary samples of arbitrary patterns are generated. For the other cases eight samples each are realized. Therefore 32 systematic patterns are realized in total. The mapping  $C \mapsto \beta$  is of the form  $f : \mathbb{R}^8 \mapsto \mathbb{R}^8$ . The desired magnetic field enhancements range from 1 up to the mean of the magnetic field enhancements of all cells at resonance (=2.18).

The parameterset of  $C_r$  can be calculated analytically. The self- and mutual-inductance can be derived from the exported admittance from simulation as follows:

$$L + M = -\frac{1}{\omega \sum_{i=0}^{n_{cell}} \Im(Y_i)} \quad (9)$$

For the calculation, the excitation ports shall be excluded. The capacitance can then be computed analogous to Eq. 7. The resonant configuration is assumed to be a good initial parameter set as it has led to a low error convergence in the one-cell case. The resonant configuration allows to reach all of the realizable magnetic field strengths (s. Fig. 10).

After optimization, the parameter set that leads to the lowest overall error is taken. In this case the parameterset that leads to the lowest overall error  $2.44 \times 10^{-7}$  is found at epoch=1652. The overall optimization took less than one minute, which emphasizes the speed of this method.

The successful realization of all 1032 desired field enhancements  $\beta$  can be demonstrated in Fig. 6 using representative samples spanning from lowest to highest error (Fig. 6 a) - e)).

For all  $\beta$ , the algorithm identified an appropriate capacitance configuration that resulted in a low error between the desired  $\beta$  and the realized  $\hat{\beta}$  (s. Fig. 6 a-d) + f). All of the realizations are achieved with a low error of  $\leq 4.4 \times 10^{-5}$ . The error distribution as shown in Fig. 6 f) is skewed towards very low errors in the  $1 \times 10^{-28}$  range. Noticably, the sample with the highest error stems from the systematic pattern domain.

As observable in Fig. 7, across all samples where a systematic pattern shall be realized, errors are low. A tendency towards higher errors can be observed when a higher  $\hat{\beta}$  or higher frequent spatially alternating patterns are desired. This is especially the case for the trough with respect to the higher field enhancement and the Hadamard patterns w.r.t. spatially varying patterns.

#### 4.3. Reconfigurable 2D MTS Optimization

A 1d-structure, as shown before, exhibits less coupling and may therefore be simpler to optimize. In order to prove the general usability of this approach, the field distribution  $|H_z|$  of an 8x8 array of resonant unit cells will be optimized in the following. The mapping  $C \mapsto |H_z|$  is of the form  $f : \mathbb{R}^{64} \mapsto \mathbb{R}^{64}$ . As shown in Eq. 7 and 9 the initial parameters for the optimization can be extracted analytically. It is not necessary to normalize on a simulation without MTS. Instead, this time  $|H_z|$  will be scaled by  $|H_z|_{ref}$  which is



extracted for one resonant cell in the centre of the structure. This will be a measure for how much we locally enhance w.r.t. to a maximum achieved by a single resonant unit cell. Therefore: One cell of the 8x8 structure will be made resonant and its  $|H_z|$  value will be extracted and taken as a reference  $|H_z|_{ref}$ . The maximum  $|H_z|$  at resonance is 0.028 A/m, the minimum  $|H_z|$  that is realized at resonance is 0.017 A/m. The maximum corresponds to approx. 60% of  $|H_z|_{ref}$ . The minimum  $|H_z|$  is extracted by calculating the fields for out-of-resonance parameters 1 and 60 pF and taking the minimum field strength of those two. This results in  $|H_z|=0.009$  A/m which corresponds to approx. 20% of  $|H_z|_{ref}$ .

In the following, four different systematic patterns will be presented:

1. Capital letters [A-Z],
2. Digits [0-9],
3. Homogenization
4. Hadamard

For the letters and digits the default font of the Python library “pillow” was used. This amounts to 45 individual samples that are scaled between 20% and 60% of  $|H_z|_{ref}$ .

The optimization converges to an error of  $2.20 \times 10^{-7}$  in epoch 1997. Overall, the optimization procedure took less than one minute. The individual samples contribute differently to the overall error.

In Fig. 8 the highest error can be found with  $14.59 \times 10^{-6}$  for a homogenized pattern with the highest desired magnetic field strength  $|\hat{H}_z| \rightarrow 63\%$  at the individual points. The sample with the lowest error can be found with a homogenized pattern with overall low desired magnetic field strength  $|\hat{H}_z| \rightarrow 33\%$  with an  $MSE=6.37 \times 10^{-34}$

In addition to the results presented in Fig. 8, Fig. 9 illustrates electromagnetic field realizations corresponding to the letters “M-E-V-I-S”. The combined field magnitudes  $|\hat{H}_z|$ , as shown in Fig. 9 a), are computed using CST MWS. The intended letter shapes are successfully generated at their respective spatial coordinates.

Although the minimum and maximum field intensities at the desired locations are consistently achieved, some regions between the specific collocation points exhibit field strengths that deviate from the minimum and maximum given during the optimization process as they are not explicitly considered.

However, within the region of interest (-105 mm to 105 mm), the letters are clearly distinguishable. These results underscore the capability of the

optimization procedure in finding good solutions for the formation of magnetic patterns.

## 5. Discussion

The convergence of gradient-descent depends on the choice of the initial parameters. In addition, given the inverse nature of the problem, one or more of the Hadamard conditions may be breached. Both shall be addressed in the following.

### 5.1. Reconfigurable Unit-Cell

To assess whether  $C_r$  is an effective starting point for the Unit-Cell optimization, a parametric sweep is conducted on 100 individual initial parameters equidistantly sampled between 0.1 pF up to 30 pF. Those individual initial parameters are then used to find solutions to 100 desired  $|H_z|$  between 0.2 to 2.3 A/m. A resulting loss plot is shown in Fig. 10.

The loss plot in Fig. 10 exhibits discontinuities and can be separated into three different parts.  $C_r = 8.39$  pF and  $C_r = 12.13$  pF are distinctive points within the plot, marking a falling or rising edge of the loss. The initial parameter with the lowest overall MSE ( $=1.26 \times 10^{-29}$ ) is close to 10.96 pF. This represents significantly better convergence compared to, for example, an initial parameter of 12.42 pF, which produced an MSE of 1.39, despite the proximity of the two values. A visualization of the error over different desired magnetic field strengths can be found in Fig. 11.

While  $C_r$  is in the range of parameters that lead to low overall errors, it is not leading to the lowest overall error within the given number of epochs.

In order to understand the discontinuous convergence behavior due to the choice of different initial parameters, it is essential to first analyze the underlying dynamics of the single split-ring resonator.

Considering Fig. 12 helps in understanding how many solutions there are (if there are any at all) and what solutions can be reached from what starting point. At one glance it is visible that when seeking any  $|H_z|$  below the global minimum and above the global maximum, the first Hadamard condition is violated as no solution exists within the given capacitance range. Within the global minimum and maximum of the loss plot in Fig. 10 multiple solutions potentially exist. Therefore the second hadamard condition is violated for some desired field strengths. Consequently, the solution that is then found depends on the initial parameter.

The solutions leading to the overall lowest error is in region II of the absolute and phase plot of  $H_z$  in Fig. 12.

- w.r.t the phase plot one can observe that the best initial parameter can be found where the change of phase is the largest
- w.r.t. the absolute plot one can observe that the best initial parameter can be found where the range of capacitances can reach all  $|H_z|$ .

Any realizable desired  $|H_z|$  is within one or more of the following capacitance ranges:

Region	$ H_z $ Range (A/m)	$C$ Range (pF)
I	$0.40 \leq  H_z  < 2.3$	$0.1 \leq C < 8.4$
II	$0.02 \leq  H_z  \leq 2.3$	$8.4 \leq C \leq 12.1$
III	$0.02 <  H_z  \leq 0.2$	$12.1 < C \leq 30.0$

Therefore only within the range  $8.39 \leq C \leq 12.13\text{pF}$  a solution for all realizable  $|H_z|$  can be found. The reason for this lies in the behaviour of gradient-descent: Vanilla gradient-descent tries to decrease the error steadily and therefore converges towards a high error because e.g. for region III in Fig. 12 and in Fig. 10 the error would have to increase before it decreases again. Vanilla gradient-descent is not able to go into the direction of higher errors. It therefore cannot overcome areas of increasing errors and will settle for a local minimum. A suitable optimizer may be able to overcome local minima but only to a certain extent.

## 5.2. Higher dimensional MTS

A notable observation in the error distribution is the presence of a long-tailed distribution (see Fig. 6 f)), which could result from unsuitable parameter initialization or from the unphysical violation of the first Hadamard condition (existant solution) by the enhancement parameter  $\beta$  in specific cases. Specifically, if  $\beta$  breaches this condition, this will likely result into increased error.

For the systematic patterns, as shown in Fig. 7, at high  $\beta$ , gradient-descent may try to converge towards a nonexistant solution, leading to increased errors. Moreover, the observation point of each individual cell is positioned

at 0.8 times their diameter. This allows nearby cells to exert an influence on the neighboring observation points. Maintaining a lower field enhancement in only one place, while concurrently sustaining a higher desired field strength in many other places could be harder to realize due to the influence of the other cells on the observation point. This also may hold for high frequent spatially varying patterns.

The selection of initial parameters critically affects the algorithm’s convergent behaviour towards an optimal solution. The initial parameter set chosen for a given field strength  $\beta$  may not be suitable when applied to different configurations, thus hindering effective optimization. Unfortunately, the discussion of initial parameters is not trivial in more dimensional cases as the number of potential initial parameters scales exponentially with  $n_{Cs}^{n_{cell}}$  with  $n_{Cs}$  denoting the number of all possible capacitance states.

Another issue becomes also apparant when using the 8x8 structure: Any real number is allowed to be a possible solution. This allows parameter sets to contain unrealistically high or low capacitance values as a solution.

In the 8x1 configuration, the final capacitance values are closer to its initial parameters (spanning from 25.36 pF to 26.44 pF) with its lowest and highest value after optimization of 24.65 pF to 35.12 pF. Conversely, in the 8x8 case, gradient-descent optimization trended towards much higher capacitance values, with a lowest value of 25.89 pF and a highest value of 66.15 pF. The initial parameters for the 8x8 configuration span from 27.78 pF to 32.9 pF. At this occasion the increase in mean and range of the initial configuration is noticable. The increased coupling therefore leads to an inherently changed behaviour of the overall resonant structure. Letting the algorithm run 20000 epochs will lead to an even further decrease of the total error but also to an increase in some capacitance configurations towards several hundred pF.

For the optimization of bounded capacitances it might make sense to reinitialize values that run out of boundary with the opposite extreme values in order to find better suited values on the otherwise not reachable side of the parameterspace. This may be subject to future research.

Additionally, the optimization is only conducted on selected collocation points. Therefore realized patterns in e.g. Fig. 9 appear not smooth. Adding more collocation points may allow a finer tuning for smoother patterns. Unfortunately this also requires better knowledge about how to set additional collocation points as all of the collocation points together need to be realizable, e.g. adding a collocation point that requires high field strengths in between two cells even though the remaining collocation points in the centre of each

cell require a low field strength probably introduces a constraint under which no good solution can be found. Adding more collocation points in the correct way may therefore be a difficult task

While satisfactory solutions have been found for many of the scenarios considered, it must be emphasized again that gradient-descent techniques do not guarantee convergence to a global minimum. Instead, the algorithm may settle into local minima.

To avoid the pitfalls of local minima, particularly in high-dimensional parameter spaces for the initial parameters, more sophisticated optimization techniques such as Bayesian optimization, as illustrated in Ref. [24], could be considered. The embedding of the simulator in a deep learning pipeline is an additional option. The framework developed here can be seamlessly integrated with such advanced techniques, allowing for efficient embedding of the forward problem within a broader optimization landscape.

## 6. Implications for Metasurfaces in MRI

In the scope of electrically reconfigurable metasurfaces for MRI the presented procedure allows to efficiently configure the electric parameters in alignment with specific imaging goals.

One exemplary use case may be the gradient coil free spatial encoding comparable to sensitivity encoding (“SENSE”). “SENSE” uses individual sensitivity profile information to allow reconstruction with undersampled phase information [25]. Different patterns would have to be realized on the metasurface in succession.

Another imaging goal could be the dynamic optimization of the electromagnetic field to enhance imaging efficiency that may be defined as a ratio of the SNR in a given region of interest to acquisition time.

The imaging efficiency can be improved by achieving the same signal-to-noise ratio (SNR) in a shorter time period or a better SNR in the same time period.

Receive coils in MRI pick up an induced voltage which can be decomposed in essentially two parts:

$$u_{ind} = u_{signal} + u_{noise}. \quad (10)$$

A properly configured MTS in the MR-bore manipulates the magnetization  $M$  in a given finite volume  $V$  as seen by the receiver coil. According to [26]

this leads to an increased  $u_{signal}$  in the receiver coil :

$$u_{signal} = 2\pi p_R f_E M V_{sample} \cos(2\pi f_E t). \quad (11)$$

$p_R$  is the coil sensitivity of the receiver coil,  $f_E$  is the excitation frequency.  $u_{noise}$  can be described by the Johnson-Nyquist-noise [26]:

$$u_{noise} = \sqrt{4k_B T_P \Delta f R_P}. \quad (12)$$

While  $R_P$  is the noise resistance of the receiver coil,  $k_B$  is the Boltzmann-constant,  $T_P$  is the particle temperature and  $\Delta f$  is the bandwidth. When using an MTS in MRI it should ideally be configured so that  $u_{signal} \propto M$  is locally increased while  $u_{noise}$  remains constant.

Fig. 13 demonstrates the local effect of MTS field shaping on the signal intensity of a low noise brain image.

It must be noted that while the signal intensity can be enhanced, the SNR will not be improved with a simple multiplication. The multiplication acts on  $u_{signal}$  as well as  $u_{noise}$  and therefore also enhances the noise. In real world application the signal-to-noise ratio will be enhanced by magnifying  $u_{signal}$  without contributing substantially to  $u_{noise}$ .

The configuration needed for the achievement of the individual imaging goals can be derived by the optimization procedure in this paper.

## 7. Conclusion

We proposed a PyTorch-based framework that accurately and efficiently models the influence of adjustable circuit parameters on the electric and magnetic field distribution. The framework supports the construction of computational graphs and automatic differentiation, which are crucial for gradient-descent-based optimization. Using this approach, we demonstrated the deliberate and direct control of the magnetic field's magnitude (specifically the component orthogonal to the resonant structure) within a reasonable range, achieving low error rates.

While investigating reconfigurable structures with one, eight and 64 individually tunable unit cells, it is found that...

- it is possible to precisely control the magnitude of the magnetic field normal to the center of each individual unit cell.

- the successful realization of desired homogenized field strengths and specific field distributions (such as peaks) at designated spatial points with low error is feasible when considering discussed constraints.

Overall, these findings provide a basis for the comprehensible, reproducible, precise and robust direct control of the magnetic field (in-silico) using reconfigurable resonant electromagnetic structures with tunable parameters. This implies that a suitable configuration for a reconfigurable MTS in MRI can be determined in order to optimize for a specific imaging goal.

The proposed approach supports the use of other gradient-based optimization methods and facilitates the embedding of the forward problem into other optimization procedures. For instance, the framework can serve as a foundation for further deep learning research, potentially being integrated into physics-informed deep learning pipelines that guides a neural network during training.

Despite these advancements, physical limitations remain, such as the potential deviation of simulations from real-world scenarios. One could establish a calibration routine that incorporates knowledge from real-world setups and accounts for differences to simulation. Additionally, the performance of gradient-descent depends on the initial parameters. Using unsuitable initial parameters may result in high error convergence due to being stuck in local minima. This may be mitigated by techniques like Bayesian optimization, deep learning, or employing a heuristic. Future research might also focus on incorporating this framework into deep learning pipelines.

A framework for the gradient-descent based optimization of resonant electromagnetic structures is successfully demonstrated and provided on [github.com](https://github.com). The suggested approach paves the way for advanced electromagnetic control strategies and provides an extendable platform for further exploration and innovation in the field.

## **Declaration of Interests**

The authors declare that they have no known competing financial interests or personal relationships that could have appeared to influence the work reported in this paper.

## Declaration of generative AI and AI-assisted technologies in the writing process

During the preparation of this work the authors partially used OpenAI's ChatGPT4o service to help in formulating. After using this service, the authors reviewed and edited the content as needed and takes full responsibility for the content of the published article.

## Acknowledgments

This research is supported by grant money received from the U Bremen Research Alliance/AI Center for Health Care, financially supported by the Federal State of Bremen.

## References

- [1] A. Shchelokova, R. Schmidt, A. Slobozhanyuk, T. Kallos, A. Webb, P. A. Belov, Enhancement of magnetic resonance imaging with metasurfaces: From concept to human trials, in: 2017 11th International Congress on Engineered Materials Platforms for Novel Wave Phenomena (Metamaterials), 2017, pp. 31–33. doi:10.1109/MetaMaterials.2017.8107800.
- [2] M. J. Freire, R. Marques, L. Jelinek, Experimental demonstration of a  $\mu=-1$  metamaterial lens for magnetic resonance imaging, Applied Physics Letters 93 (23) (2008) 231108. doi:10.1063/1.3043725.  
URL <https://aip.scitation.org/doi/full/10.1063/1.3043725>
- [3] M. J. Freire, L. Jelinek, R. Marques, M. Lapine, On the applications of  $\mu r=-1$  metamaterial lenses for magnetic resonance imaging, Journal of Magnetic Resonance 203 (1) (2010) 81–90. doi:10.1016/j.jmr.2009.12.005.  
URL <https://www.sciencedirect.com/science/article/pii/S1090780709003607>
- [4] J. M. Algarín, M. J. Freire, F. Breuer, V. C. Behr, Metamaterial magnetoinductive lens performance as a function of field strength, Journal of Magnetic Resonance 247 (2014) 9–14. doi:10.1016/j.jmr.2014.08.006.



- [5] E. A. Brui, A. V. Shchelokova, M. Zubkov, I. V. Melchakova, S. B. Glybovski, A. P. Slobozhanyuk, Adjustable Subwavelength Metasurface-Inspired Resonator for Magnetic Resonance Imaging, *physica status solidi (a)* 215 (5) (2018) 1700788. doi:10.1002/pssa.201700788. URL <https://onlinelibrary.wiley.com/doi/abs/10.1002/pssa.201700788>
- [6] A. V. Shchelokova, A. P. Slobozhanyuk, I. V. Melchakova, S. B. Glybovski, A. G. Webb, Y. S. Kivshar, P. A. Belov, Locally enhanced image quality with tunable hybrid metasurfaces, *Physical Review Applied* 9 (1) (2018) 014020. doi:10.1103/physrevapplied.9.014020.
- [7] E. Stoja, S. Konstandin, D. Philipp, R. N. Wilke, D. Betancourt, T. Bertuch, J. Jenne, R. Umathum, M. Günther, Improving magnetic resonance imaging with smart and thin metasurfaces, *Scientific Reports* 11 (1) (2021) 16179. doi:10.1038/s41598-021-95420-w. URL <https://www.nature.com/articles/s41598-021-95420-w>
- [8] T. Hand, S. Cumber, Controllable magnetic metamaterial using digitally addressable split-ring resonators, *IEEE Antennas and Wireless Propagation Letters* 8 (2009) 262–265. doi:10.1109/lawp.2009.2012879.
- [9] G. Oliveri, D. H. Werner, A. Massa, Reconfigurable electromagnetics through metamaterials—a review, *Proceedings of the IEEE* 103 (7) (2015) 1034–1056. doi:10.1109/jproc.2015.2394292.
- [10] Q. He, S. Sun, L. Zhou, Tunable/reconfigurable metasurfaces: Physics and applications, *Research* 2019 (Jan. 2019). doi:10.34133/2019/1849272.
- [11] H. Wang, H.-K. Huang, Y.-S. Chen, Y. Zhao, On-demand field shaping for enhanced magnetic resonance imaging using an ultrathin reconfigurable metasurface, *VIEW* 2 (3) (2021) 20200099. doi:10.1002/viw.20200099.
- [12] M. Lippke, E. Stoja, D. Philipp, S. Konstandin, J. Jenne, T. Bertuch, M. Gunther, Investigation of a digitally-reconfigurable metasurface for magnetic resonance imaging, in: *2022 52nd European Microwave Conference (EuMC)*, IEEE, 2022. doi:10.23919/eumc54642.2022.9924424.
- [13] E. Stoja, D. Philipp, S. Konstandin, J. Jenne, T. Bertuch, M. Günther, Reconfigurable metasurfaces and new imaging paradigms in magnetic

- resonance imaging, in: 2023 17th European Conference on Antennas and Propagation (EuCAP), IEEE, 2023. doi:10.23919/eucap57121.2023.10132982.
- [14] J. Müller, M. Falchi, E. Stoja, S. Konstandiri, M. Gunther, D. Brizi, P. Usai, A. Monorchio, D. Philipp, Deep-learning optimized reconfigurable metasurface for magnetic resonance imaging, in: 2024 18th European Conference on Antennas and Propagation (EuCAP), IEEE, 2024. doi:10.23919/eucap60739.2024.10500954.
- [15] M. Eisterer, The significance of solutions of the inverse biot–savart problem in thick superconductors, *Superconductor Science and Technology* 18 (2) (2004) S58–S62. doi:10.1088/0953-2048/18/2/013.
- [16] R. Teyber, L. Brouwer, J. Qiang, S. Prestemon, Inverse biot–savart optimization for superconducting accelerator magnets, *IEEE Transactions on Magnetics* 57 (9) (2021) 1–7. doi:10.1109/tmag.2021.3092527.
- [17] A. Beqiri, J. W. Hand, J. V. Hajnal, S. J. Malik, Comparison between simulated decoupling regimes for specific absorption rate prediction in parallel transmit MRI, *Magnetic Resonance in Medicine* 74 (5) (2014) 1423–1434. doi:10.1002/mrm.25504.
- [18] U. Zanovello, F. Seifert, O. Bottauscio, L. Winter, L. Zilberti, B. Ittermann, CoSimPy: An open-source python library for MRI radiofrequency coil EM/circuit cosimulation, *Computer Methods and Programs in Biomedicine* 216 (2022) 106684. doi:10.1016/j.cmpb.2022.106684.
- [19] D. Brizi, A. Monorchio, An analytical approach for the arbitrary control of magnetic metasurfaces frequency response, *IEEE Antennas and Wireless Propagation Letters* 20 (6) (2021) 1003–1007. doi:10.1109/lawp.2021.3069571.
- [20] M. Kozlov, R. Turner, Fast MRI coil analysis based on 3-d electromagnetic and RF circuit co-simulation, *Journal of Magnetic Resonance* 200 (1) (2009) 147–152. doi:10.1016/j.jmr.2009.06.005.
- [21] CST AG, CST Studio Suite 2024 Help, Dassault Systèmes, accessed: 2024-07-03 (2024). URL <https://www.3ds.com/products-services/simulia/products/cst-studio-suite/>

- [22] ZMT Zurich MedTech AG, Sim4Life, ZMT Zurich MedTech AG, accessed: 2024-07-03 (2024).  
URL <http://www.zmt.swiss/sim4life/>
- [23] D. P. Kingma, J. Ba, Adam: A method for stochastic optimization (2014). doi:10.48550/ARXIV.1412.6980.
- [24] R. Antonova, J. Yang, K. M. Jatavallabhula, J. Bohg, Rethinking optimization with differentiable simulation from a global perspective (2022). doi:10.48550/ARXIV.2207.00167.
- [25] K. P. Pruessmann, M. Weiger, M. B. Scheidegger, P. Boesiger, Sense: sensitivity encoding for fast mri., *Magnetic resonance in medicine* 42 (1999) 952–962.
- [26] T. Knopp, T. M. Buzug, *Magnetic Particle Imaging: An Introduction to Imaging Principles and Scanner Instrumentation*, Springer Berlin Heidelberg, 2012. doi:10.1007/978-3-642-04199-0.

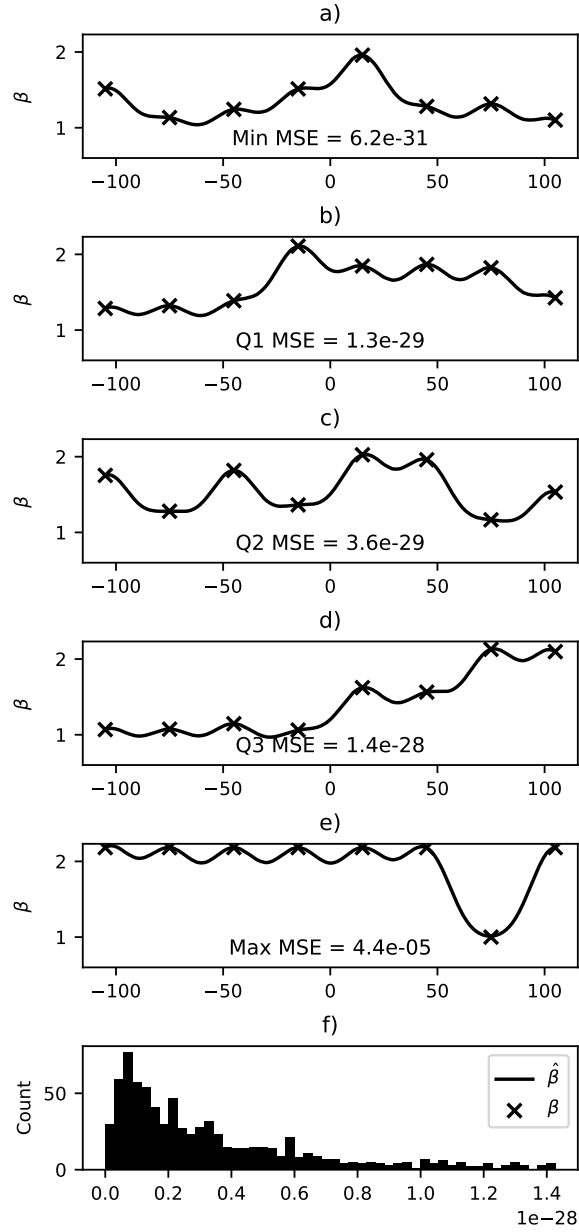


Figure 6: Distribution plot of the magnetic field enhancement for the 8x1 case. Individual samples that are realized with lowest a), first-quartile b), median c), third-quartile d) and the highest error e) are shown. The desired magnetic field enhancement  $\beta$  is compared and quantified to the realized magnetic field enhancement  $\hat{\beta}$  using the MSE at the collocation points. In f) a distribution plot shows the error distribution for all 1032 samples in the range from zero to the third quartile. There is at least one outlier with an error of  $4.4 \times 10^{-5}$ .

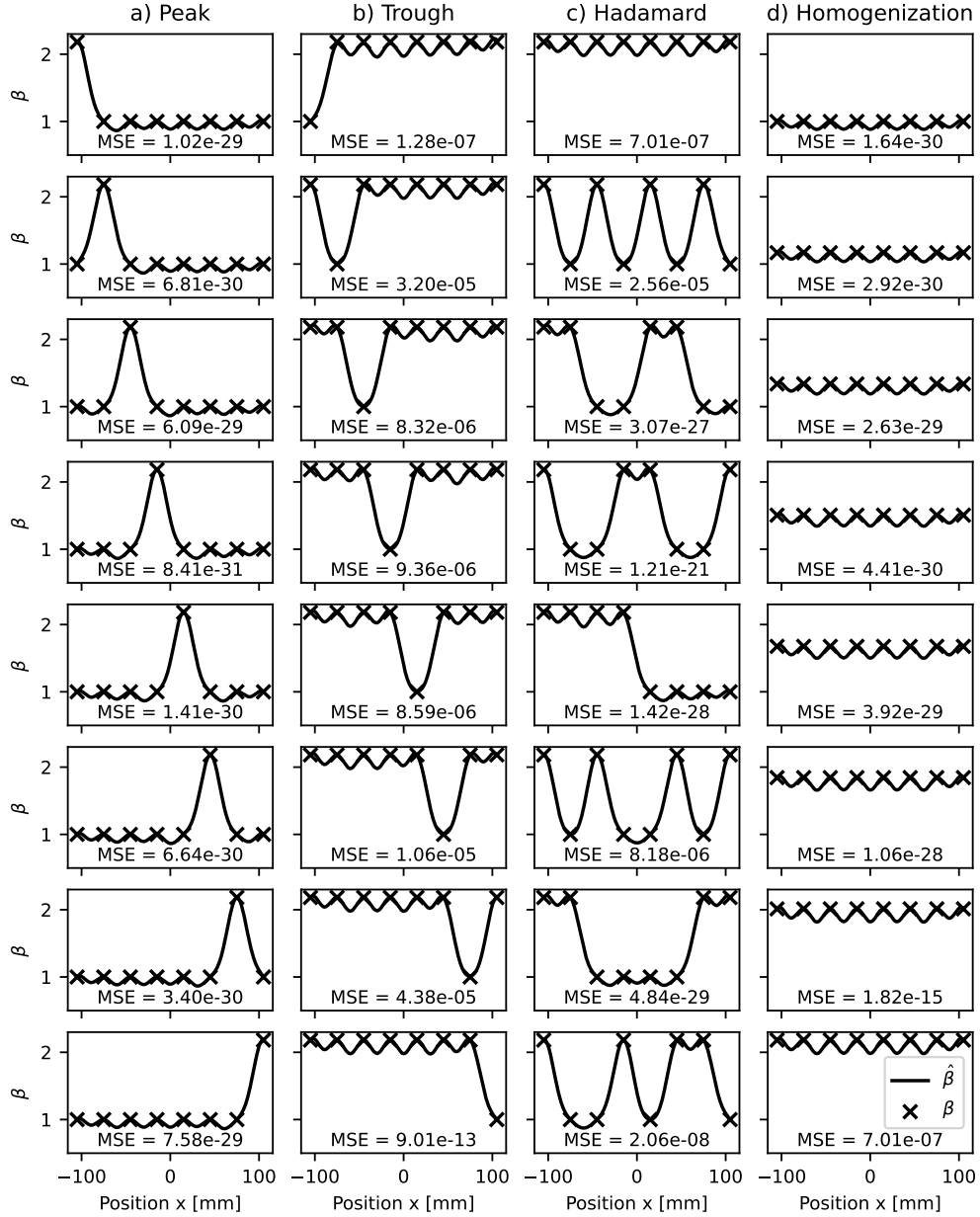


Figure 7: Demonstration of 32 different systematic desired and optimized magnetic field enhancement patterns  $\beta$  with a low error of less than  $4.4 \times 10^{-5}$  to  $\hat{\beta}$ . In a) a shifting peak going from the left most centre of the cell to the right most centre of the cell is shown. In b) the  $\beta$  is inverted. A shifting trough is shown. In c) Hadamard patterns are realized. In d) different strengths of homogenization are shown.

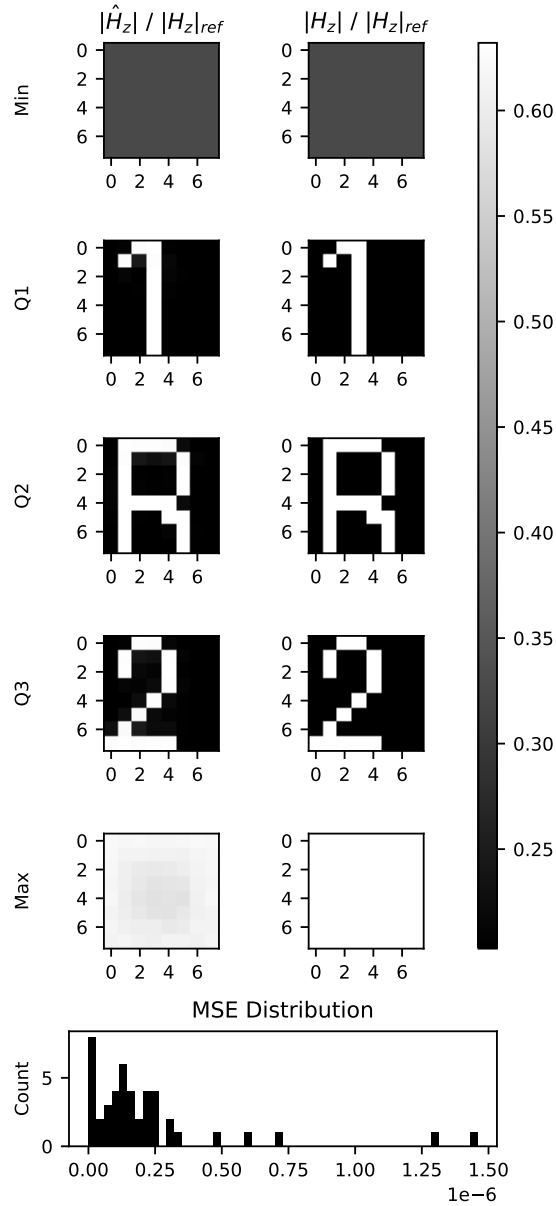


Figure 8: Distribution plot of the magnetic field strength  $|H_z|$ . Samples realized with lowest (Min), first-quartile (Q1), median (Q2), third-quartile (Q3) and the highest error (Max) are shown. The desired magnetic field enhancement  $|H_z|$  is compared and quantified to the realized magnetic field enhancement  $|\hat{H}_z|$  using the MSE at the collocation points. At the bottom a distribution plot shows the error distribution for all 45 samples in the range from zero to the maximum error.

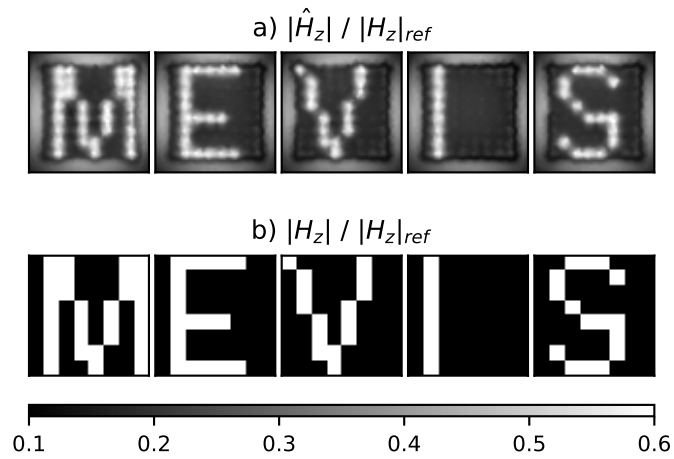


Figure 9: Demonstration of individual letters “M-E-V-I-S” realized on the 8x8 array. a) shows the  $|\hat{H}_z|$  as realized in CST MWS. A field-of-view of 300x300 mm is shown. The 8x8 Array has an extent of 220x220 mm and is centered in the field-of-view. The plane is 0.8 times underneath the diameter of the unit cell. Therefore, in this view, the edges of the array are clearly visible. b) shows  $|H_z|$  as desired by the user in the collocation points. Therefore this is an 8x8 px array comparable to the samples shown in Fig. 8.

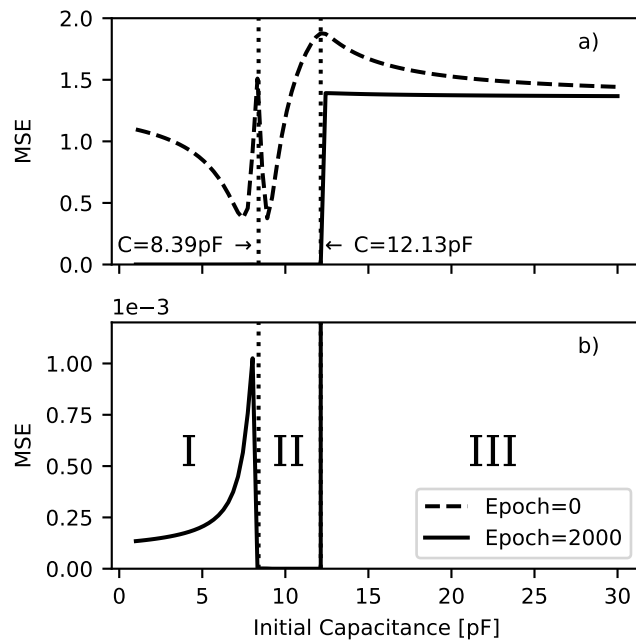


Figure 10: The initial capacitance configuration of the one unit cell setup is swept from 0.1 pF up to 30 pF and then used for optimization. The losses at the last epoch (epoch=2000) are visualized. The loss plot can be divided into three individual regions (I, II, III). The capacitances in region II lead to the overall lowest error while capacitances in region III lead to the highest overall error.



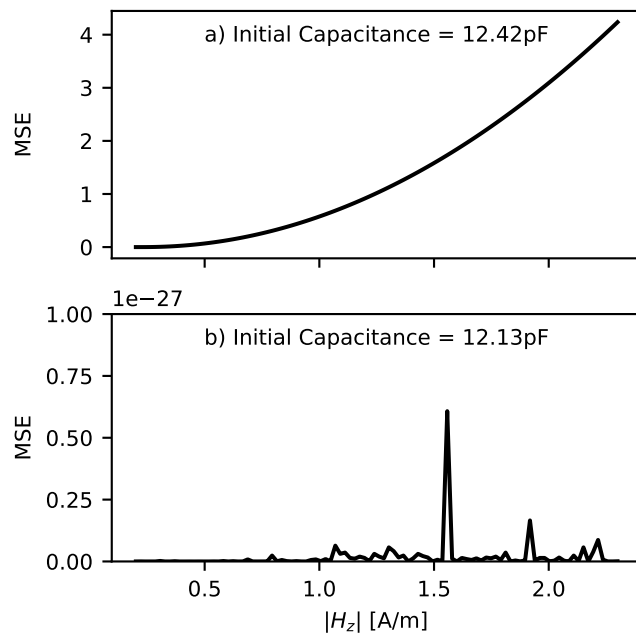


Figure 11: Difference in final error (epoch=2000) per sample between the initial capacitance set to 12.13 pF in a) which results in the highest overall error and initial capacitance set to 12.42 pF in b) which results in one of the lowest overall errors. For the majority of samples there is a more than  $1 \times 10^{-27}$  difference in scale w.r.t. the errors.

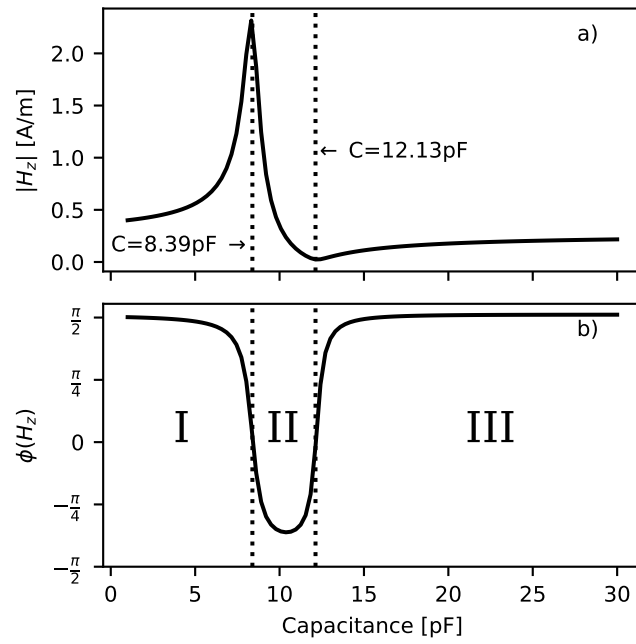


Figure 12: Variation of the capacitance and the effect on the a) absolute and b) phase of the magnetic field  $|H_z|$  for a single-cell setup. The plot illustrates the nonlinear relationship observed, highlighting the key points where significant changes in magnetic field w.r.t. capacitance occur. Only capacitances in region II can realize all possible desired magnetic field strengths. This correlates with low overall errors in Fig. 10.

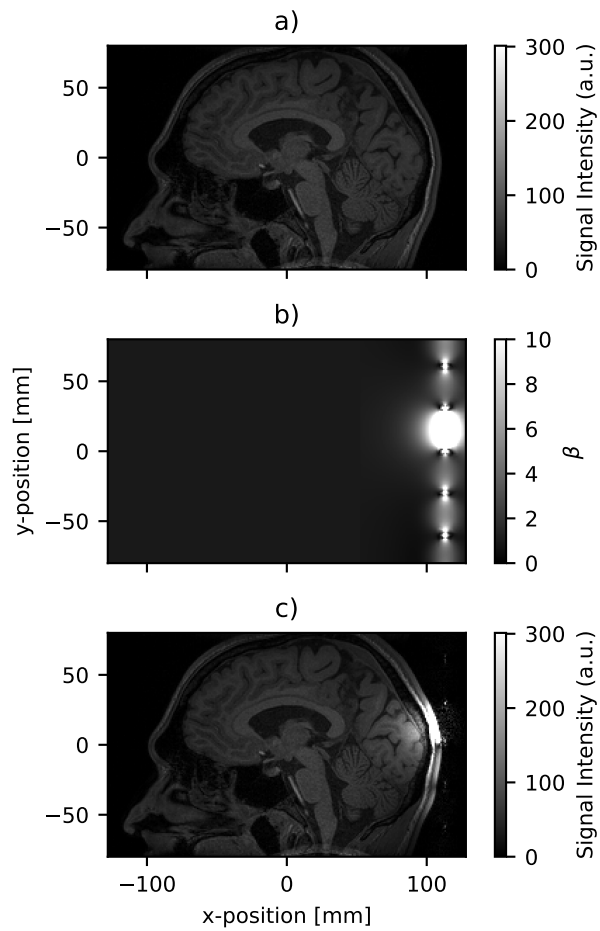


Figure 13: Demonstration of signal intensity enhancement in a reconstructed MR brain image by field shaping of an 8x1 MTS. a) shows the reconstructed MR brain image without field enhancement. b) shows the field enhancement  $\beta$  of the z-component in the plane that is cutting longitudinally through the center of the 8x1 MTS. By combining a) and b) in c), a local enhancement of the signal intensity can be observed.